HHS Public Access

Author manuscript

Phys Med Biol. Author manuscript; available in PMC 2024 May 19.

Published in final edited form as:

Phys Med Biol. ; 66(15): . doi:10.1088/1361-6560/ac1246.

Improvements in beam's eye view fiducial tracking using a novel multilayer imager

T C Harris[1,2,3], **J Seco**[2,3], **D Ferguson**[4], **M Jacobson**[1], **M Myronakis**[1], **I Valencia Lozano**[1], **M Lehmann**[5], **P Huber**[5], **R Fueglistaller**[5], **D Morf**[5], **H J Mamon**[1], **J D Mancias**[1], **N E Martin**[1], **R I Berbeco**[1]

[1]Department of Radiation Oncology, Brigham and Women's Hospital, Dana Farber Cancer Institute and Harvard Medical School, Boston, MA, United States of America

[2]BioMedical Physics in Radiation Oncology, DKFZ, Heidelberg, Germany

[3]Department of Physics, University of Heidelberg, Heidelberg, Germany

[4]Department of Radiation Oncology, University of California San Francisco, San Francisco, CA, United States of America

[5]Varian Medical Systems, Baden-Dattwil, Switzerland

Abstract

Purpose.—Electronic portal image devices (EPIDs) have been investigated previously for beams-eye view (BEV) applications such as tumor tracking but are limited by low contrast-to-noise ratio and detective quantum efficiency. A novel multilayer imager (MLI), consisting of four stacked flat-panels was used to measure improvements in fiducial tracking during liver stereotactic body radiation therapy (SBRT) procedures compared to a single layer EPID.

Methods.—The prototype MLI was installed on a clinical TrueBeam linac in place of the conventional DMI single-layer EPID. The panel was extended during volumetric modulated arc therapy SBRT treatments in order to passively acquire data during therapy. Images were acquired for six patients receiving SBRT to liver metastases over two fractions each, one with the MLI using all 4 layers and one with the MLI using the top layer only, representing a standard EPID. The acquired frames were processed by a previously published tracking algorithm modified to identify implanted radiopaque fiducials. Truth data was determined using respiratory traces combined with partial manual tracking. Results for 4- and 1-layer mode were compared against truth data for tracking accuracy and efficiency. Tracking and noise improvements as a function of gantry angle were determined.

Results.—Tracking efficiency with 4-layers improved to 82.8% versus 58.4% for the 1-layer mode, a relative improvement of 41.7%. Fiducial tracking with 1-layer returned a root mean square error (RMSE) of 2.1 mm compared to 4-layer RMSE of 1.5 mm, a statistically significant ($p < 0.001$) improvement of 0.6 mm. The reduction in noise correlated with an increase in successfully tracked frames ($r = 0.913$) and with increased tracking accuracy (0.927).

tharris@bwh.harvard.edu .

Conclusion.—Increases in MV photon detection efficiency by utilization of a MLI results in improved fiducial tracking for liver SBRT treatments. Future clinical applications utilizing BEV imaging may be enhanced by including similar noise reduction strategies.

Keywords

EPID; beams eye view; tumor tracking

1. Introduction

Electronic portal imaging devices (EPIDs) are available on most linear accelerators, replacing film cassettes for acquiring MV portal images for radiotherapy localization and verification (Herman et al 2001). Over time, a number of additional clinical applications for MV imaging have been developed. Of particular interest is the *cine* mode, in which the EPID acquires sequential images of the treatment field after it has exited the patient.

MV cine imaging, also sometimes referred to as 'beam's-eye-view' (BEV) imaging, offers several advantages in comparison to on-board orthogonal kV imaging. Importantly, the patient receives no additional imaging dose; for real-time applications, continuous kV fluoroscopy dose may become substantial (Murphy et al 2007). MV cine images also show the actual anatomy undergoing irradiation in real-time, rather than an orthogonal view. Each individual MV cine frame is two-dimensional, which can be sufficient since the third dimension, depth, is dosimetrically not as significant for high energy x-ray irradiation. Despite these benefits, clinical implementation of EPIDs to manage patient motion has been hindered by the inherently low contrast of MV imaging and the relatively low detective quantum efficiency (DQE) of currently used EPIDs (Antonuk 2002).

Advanced real-time applications enabled by MV *cine* imaging include treatment verification and monitoring. BEV automated tracking of implanted fiducials (Keall et al 2004, Park et al 2009) during beam delivery helps ensure accurate dose delivery while potentially enabling a more conformal treatment. However, dynamic modulation of the treatment aperture and direction complicate the task of tracking fiducial locations. Some researchers have directly addressed the issue of MLCs obscuring fiducials (Azcona et al 2013, Yue et al 2011, Hu et al 2018). Others have developed indirect methods such as using combined imaging modalities with kV (Wiersma et al 2008, Cho et al 2011), modifying the MLCs during treatment planning to optimize fiducial visibility (Happersett et al 2019), and determining best fiducial placement to maximize frames containing a fiducial (Ma et al 2018).

There has been extensive research dedicated to improving EPID performance. Some investigations have focused on novel scintillator materials (Hu et al 2019) and scintillator construction, such as structured phosphors (Zhao et al 2004) and pixelated scintillators (Star-Lack et al 2015). Stacking several layers of current generation components is an economical and relatively practical approach. This strategy boosts photon collection efficiency without an increase in Swank noise (Swank 1973). Using multiple detection layers provides a substantial elevation in DQE while preserving field of view and spatial resolution (Harris 2020).

Characterization of the MV imaging panel used to acquire data for the present study has been previously published (Harris et al 2020). Here, we extend our prior work by studying the impact of this novel multi-layer EPID on fiducial tracking in BEV images acquired during clinical SBRT procedures. Previously, we demonstrated a 1.87 fold increase in the contrast-to-noise ratio of a fiducial to surrounding liver tissue when using a 4-layer EPID compared to 1-layer. The objective of the present study was to study how this enhanced performance translates to the clinical application of fiducial tracking, in terms of both fiducial tracking accuracy and efficiency, in the presence of unfavorable anatomic arrangements or treatment beam apertures.

2. Materials and method

2.1. Multi-layer imager (MLI)

We used a novel MLI comprised of four identical layers of: (1) a copper sheet to convert photons to secondary electrons, and shield against low energy scattered radiation. (2) Terbium-doped gadolinium oxysulfide (GOS) as a scintillator to convert radiation to optical photons. (3) Hydrogen doped amorphous silicon deposited on a glass substrate to form a pixelated array of photodiode thin film transistors to detect the optical photons. This flat-panel imager's composition is similar to current commercially available EPIDs, although the MLI's scintillator has a thickness of 0.436 mm (200 mg cm^{-2}) per layer. This thickness matches what is available on Varian's Halcyon clinical treatment platform but is thicker than the AS-1200 scintillator (0.290 mm, 113 mg cm^{-2}) available on most other Varian linacs.

The MLI's firmware permits it to run in 4-layer mode—in which the response of each layer is averaged together—or in 1-layer mode utilizing just the top layer, thus approximating a standard EPID. In our previously published work, the DQE(0) for 6 MV was found to be 1.7% for the AS-1200, 2.6% for the MLI 1-layer mode, and 9.7% for the MLI 4-layer mode, a 5.7× increase in performance over the standard commercially available model. Both 4-layer and 1-layer acquisition modes were used in this study to compare the performance difference of a MLI to a standard single-layer EPID.

2.2. Data acquisition

Clinical images were collected under Dana-Farber Cancer Institute IRB approval (DFCI#18–517). The MLI was placed inside the standard AS-1200 housing and collision frame, mounted onto a TrueBeam's MV imager arm, and connected to the standard optical data cable. A computer with a frame grabber card was connected to an output jack of the TrueBeam's XI node to collect the stream of image frames.

BEV images during SBRT were passively acquired for six patients with liver metastases (four with one metastasis; two with two metastases). Five of the six patients had tumors in the right lobe, while the sixth patient had one lesion in the right lobe and one in the left lobe. Patients received 5 fraction SBRT using 2–3 VMAT arcs delivering per fraction doses ranging from 900 to 1200 cGy. Beam energy was 6 MV in flattening-filter-free (FFF) mode, with the beam calibrated to deliver 1 cGy M^{-1} U^{-1} at d_{max} with a 10 cm × 10 cm open field, 100 cm SAD. Patients received both a standard helical planning CT and a 4D CT

using Varian's RGSC gating system. Treatment plans were generated routinely, and without consideration for the imaging study. The MLI was extended to 180 cm source to imager distance (SID) to ensure adequate patient clearance. Acquired images were flood field, dark field, and pixel defect map corrected. On average, 10.1 frames per second were passively gathered during patients' beam deliveries.

Patients had three gold cylindrical fiducials (diameter 0.8 mm, length 3 mm, Fiduciary Marker Kit, Best Medical International) implanted in their PTVs, except for two of the patients who had two separate lesions. Those two patients had two fiducials implanted in each of their two PTVs, for a total of four implanted markers each. Fiducials were later calculated to have an average spacing of 3.3 cm +/− 1.4 cm. Patients received an initial setup CBCT and triggered kV images every 5 degrees of rotation to continue verifying positioning, as is our standard of care. Using RGSC, 4 of the patients were monitored by 'safety gating' and 2 of the patients were treated using light inspiration breath hold.

BEV images were acquired for each patient across two treatment fractions, each consisting of 2–3 treatment arcs. Full 360 degree arcs could not be delivered because the treatment isocenters were located in the liver and thus too lateral in the patient to avoid collisions. Therefore, gantry arcs started at 181 degrees and terminated from 320 to 30 degrees, after which the couch was temporarily shifted laterally to allow the gantry to pass without patient collision, followed by treatment from the contralateral side. One fraction was performed with the MLI in 4-layer acquisition mode, and the other fraction with the MLI in 1-layer acquisition mode. The treatment delivery procedure was not altered to accommodate the imaging study other than the several seconds needed to extend the MV panel at the start of the treatment fraction.

2.3. Tracking algorithm

The fiducial tracking algorithm used in this study is a modification of previously published work from our group, initially designed for marker-less tracking (Ferguson et al 2020) and will be briefly summarized here.

The tracking algorithm automatically detects features of interest in 2D image frames and tracks those features while visible within the aperture. Each image frame is initially masked by the collimator jaw settings and the MLC positions, as well as a region around them to exclude any gradient near a boundary. After masking, candidate features for tracking are described by a cluster of templates generated along lines of high local variance. The cluster of templates helps to encode the shape of the feature. Template matching is performed on subsequent images using the calculated normalized cross-correlation (NCC) on the variance map. Templates are scored by a weighted combination of multiple factors: the NCC value of the template, divergence from the original relative template orientations, and the average stability of the templates (how often they contribute to successful feature tracking).

Although the algorithm was initially designed for tracking tumors in lung directly, radiopaque fiducials create an area of high local variance on the images and thus should be identified easily. In addition, we made modifications to the code to optimize it for fiducial tracking. The contour created by the templates was evaluated for shape and spatial

dimensions, identifying if the feature was shaped like a fiducial—either circular 'head-on,' cylindrical from the side, or some eccentric angle between the two. The tracker was also provided with the isocenter and fiducial coordinates from the planning CT, which—after applying a rotation matrix based on the gantry angle and a scaling factor based on the SID—provides an expected fiducial position on each frame. The search region centered on these expected locations is expanded by double the range of motion observed on the treatment planning 4D CT scan. For the patients in this study the range of motion was between 7 and 10 mm, so the region of interest was 14–20 mm. Figure 1 shows an example of a pair of frames using matched positions in the same arc from a patient's fraction captured using the MLI's 4-layer mode and a fraction captured using 1-layer mode. The green circles show the search area for each fiducial, the asterisks are templates generated at a fiducial's initial tracked location after a frame with unsuccessful tracking, and the blue arrows point to the corresponding templates' current tracked location.

Generating 'truth data' with which to compare the tracked fiducial locations was performed by combining external surrogate breathing data with some manually tracked images. Each treatment arc generated hundreds of image frames, so performing manual tracking on each frame was not practical. Since every patient had a breathing trace recorded during radiation delivery, we were able to use the trace as a surrogate for relative fiducial location. The correlation of surface markers with internal tumor motion has been the topic of extensive research (Gierga et al 2005, Ionascu et al 2007, Fayad et al 2011, Lu et al 2015). In our study, 14 frames near the beginning of the treatment arc and 14 frames near the end of the treatment arc were selected based on the visibility of the fiducials within the aperture. The fiducial locations in these frames were identified manually and the time points matched to the corresponding time point of the breathing trace (figure 2). In order to match the TrueBeam time stamps with the acquired images, the in-treatment triggered kV images were used to temporally match the breathing trace with the collected frames. The kV images were acquired at known recorded gantry angles, so their time stamps could be compared with the metadata time of the MV images acquired at the same gantry angle, and any discrepancy appropriately compensated for.

The tracking algorithm reads in the collected images, searches for fiducials, and compares the found location to the derived truth data for error analysis. The algorithm also estimates an expected number of frames for which a fiducial might be visible by comparing the expected fiducial location at each frame with the MLC coverage for that location in that frame. The number of frames with successful tracking of a particular fiducial are compared to the theoretical maximum number of trackable frames to calculate an efficiency metric. Paired two sample for means T-tests were used to assess the significance of the difference in tracking error and efficiency between 1-layer acquisitions and 4-layer acquisitions.

2.4. Analysis

We studied several conditions for the differences in tracking efficiency and accuracy between the 4-layer and 1-layer modes. One hypothesis was that the tracking efficiency would be correlated with gantry angle, meaning that certain ranges of the treatment arcs were better suited for tracking, in general, and that some low efficiency angles could be

improved with the 4-layer imaging. In addition, dose rate as a function of gantry angle was cataloged for all acquired frames using MU per frame as a proxy for dose rate, given that the frame grabber card acquired images at a stable 10.1 frames per second. We sought to determine if dose/frame impacted the tracking efficiency and could likewise be overcome by the 4-layer imager.

Our second main hypothesis was that image noise would be correlated to tracking efficiency such that reduction in noise would lead to better efficiency. Image noise at a particular gantry angle is a function of dose-rate of the source, radiological depth of the subject and DQE of the imaging panel. Using the same fiducial location prediction technique explained in section 2.3, the image noise in the search location of the seeds was calculated. First, a median-filtered version of each frame was subtracted from the corresponding frame to remove deterministic background non-uniformities. A 5 × 5 median pixel filter was used for this step, which outputs the median pixel value in a 5 × 5 pixel neighborhood around the input pixel. Second, the MLCs were masked on the image. Third, the image was cropped to the fiducial search area. Finally, the noise was determined from the standard deviation of the pixel values unless the MLCs obscured the data, in which case the data point was omitted. This calculation was performed for every fiducial across all of the patient image frames for both 1-layer and 4-layer cases.

3. Results

A total of 23 242 clinical BEV MV image frames were successfully captured from the six liver SBRT patients, excluding frames that were blank due to manual triggering and gating. For each patient, data was acquired during two fractions: one fraction with the MLI in 4-layer acquisition mode and one fraction with it in 1-layer acquisition mode. Continuous saving of the image data stream was triggered manually to occur independent of the treatment status, although the tracking algorithm ignores image frames when the MV beam is not on (as defined by the BeamOn flag in each image's metadata).

The tracked position of each fiducial in each arc was compared to the truth data location and the root mean square error (RMSE) in the X direction, Y direction, and total error calculated. Including the data from all fiducials in every arc in every patient, the 1-layer RMSE was 2.1 mm and the 4-layer RMSE 1.5 mm, an improvement of 0.6 mm ($p < 0.001$). Patient by patient data is shown in table 1.

The number of successfully tracked frames of each fiducial of each arc of each patient was compared to the theoretical maximum number of frames for which tracking was possible, i.e. when at least one fiducial was not covered by the MLCs. This ratio of successful tracking frames to total frames was defined as the 'tracking efficiency'. The tracking algorithm was able to return results for 58.4% of the 1-layer data image frames and 82.8% of the 4-layer data image frames, an absolute increase of 24.4% ($p < 0.001$).

The gantry angle distribution of where successful tracking occurred was analyzed. Due to the laterality of the liver, many of the patients did not have arcs covering the range from 30 to 180 degrees. Figure 3 shows the distribution for a single arc of a patient's treatment when

the MLI is in 4-layer mode and the corresponding arc in 1-layer mode. Some angles also have no tracking due to MLC interference. Of note, the increase in tracking from multi-layer acquisition does not appear homogenously distributed. The net increase of tracked frames for the 4-layer mode displays similar trends for all patients with a peak centered around 330 degrees gantry angle and a valley centered around 250 degrees gantry angle (figure 4).

The average MU per frame as a function of gantry angle was evaluated for all collected frames in the cohort of patients (figure 5(a)). The frame grabber acquired images at a stable rate of 10.1 frames per second, meaning the maximum MU per frame is roughly 2.3, given the nominal 6FFF dose rate of 1400 MU min^{-1}. The delivered dose rate was stable except for noticeable dips near gantry 30, 130, and 330. The image noise in the search region around each fiducial across all data was determined as described in section 2.4. Data from fiducials obscured by MLCs were omitted and defined as ‘untrackable’. The average decrease noise as a function of gantry angle is shown in figure 5(b). There is a peak centered around the gantry angle of 330 degrees. Figure 6 combines the plots of the net tracking increase by gantry angle and the noise per gantry angle. There is a strong correlation between image noise and improved tracking with the 4-layer mode of MLI (r = 0.913). The correlation is also strong (r = 0.927) when considering the relationship between image noise and tracking accuracy improvement. Figure 7 replots figures 6(a) and (b) as a function of noise decrease instead of gantry angle.

4. Discussion

The 4-layer MLI provides statistically significant improvement in tracking accuracy and efficiency versus 1-layer acquisition. Previous work has shown that tracking performance is generally limited by quantum noise, which is dominated by DQE (Hu et al 2017). This is demonstrated in the superior tracking performance of the higher DQE imaging mode, i.e. 4-layer acquisition. The more than five-fold increase in DQE, utilizing four layers, led to a 41.7% relative increase in tracking efficiency and statistically significant increase in tracking accuracy, as well. Future studies could investigate fiducials of different diameters and lengths, as well as other marker types such as gold anchors.

As discussed in prior work by our group (Harris et al 2020), improved tracking performance is primarily driven by improved noise power spectrum, with the minor decrease in modulation transfer function having negligible impact on the ability to track fiducials. However, creating a single layer EPID with a GOS layer four times thicker likely would not yield similar results. A prior study demonstrated decreasing returns for GOS layers thicker than 0.500 mm, due to signal power degradation offsetting the decrease in noise power (Hu et al 2017). Furthermore, a thicker scintillator layer creates additional optical photon spread, leading to optical Swank noise (Swank 1973). The MLI architecture used in this study allows an effectively thicker scintillator without increased optical Swank noise.

MLI may offer the additional advantage of detecting errors in patient positioning. For example, during patient treatment for this study, there was one fraction during 4-layer acquisition when an unacceptable change in position was detected on the treatment console using the triggered-kV images, so the MV frame grabber was halted during the repeat CBCT

and then re-started for the acquisition of the remainder of that arc. The two parts of the arc were later stitched together. The MV data for this particular arc was later reviewed, and one of the three fiducials was visible in frame when the kV images detected a misalignment. The fiducial position was being tracked with an accuracy or 1.1 mm or less, suggesting that the MLI may have detected the setup issue as well.

A pattern of greatly improved tracking with the 4-layer mode around a gantry angle of 330 degrees emerged during the analysis (figure 6). Investigating this further, it was noted that the treatment beams often pass through both the fiducials and the spine from this direction. The MLCs tend to be close to the fiducials, blocking the spine when possible. This condition likely results in relatively higher image noise, which would limit tracking with the 1-layer mode more than with the 4-layer mode.

Across all of the gantry angles, in regions where there is more noise around the fiducials, the 4-layer panel is able to track more frames than the 1-layer mode. In angular regions where there is less noise in the images and tracking is relatively easier, the advantage of higher detector efficiency is less prominent. Figure 7 suggests that for the tracking system analyzed in this study, there may be a threshold in noise improvement needed before performance increases. Performance improvements appear to taper off as noise decreases, likely reflecting that accuracy and efficiency can only be improved so much. More data is needed for further quantification, and more tracking systems would need to be studied before generalizing this observation.

Monitoring of intrafraction target motion can improve treatment delivery accuracy for radiation therapy (Bertholet et al 2019), particularly in anatomical regions sensitive to respiratory motion (Keall et al 2006). Without active monitoring, there are other strategies to address target motion. For example, a 4D CT can help quantify the typical range of intrafraction motion (Mageras et al 2004) but does not provide information at the time of treatment. Methods for minimizing motion include active breathing control (Wong et al 1999), various breath hold methods (Boda-Heggemann et al 2016), and abdominal compression (Heinzerling et al 2008). However, these tools do not provide feedback on the actual target position and motion during treatment.

BEV imaging with the MV beam during treatment delivery can be used to verify the above methods of motion mitigation without contributing additional imaging dose to the patient. In-treatment patient imaging with current conventional MV imagers has drawbacks, however, such as poor contrast and DQE, making clinical adoption challenging. Additionally, MLC modulation and gantry rotation during beam delivery further complicate fiducial identification. In this study, we have sought to demonstrate that increased photon detection efficiency through detector modifications reduces image noise and thereby improves both tracking efficiency and tracking accuracy. While the 4-layer MLI used in the study has achieved those goals, other innovations will be necessary in order to overcome remaining challenges, such as MLC obstructions.

5. Conclusion

BEV imaging with a novel MLI demonstrated increased tracking efficiency and tracking accuracy compared to a reference single layer imager for clinical liver SBRT treatments. The improved performance is highly correlated with the reduction in image noise associated with the photon detection efficiency of each imaging panel. For future innovations, including MV imaging to monitor radiotherapy treatments, incorporating high efficiency detectors, like the MLI used in this study, is recommended.

Acknowledgments

This work was supported in part by award number R01CA188446 from the National Institutes of Health. The authors would also like to thank the therapists on the Brigham and Women's Silver linac for their assistance with this project.

References

Antonuk LE 2002 Electronic portal imaging devices: a review and historical perspective of contemporary technologies and research Phys. Med. Biol. 47 R31–65 [PubMed: 11936185]

Azcona JD, Li R, Mok E, Hancock S and Xing L 2013 Development and clinical evaluation of automatic fiducial detection for tumor tracking in cine megavoltage images during volumetric modulated arc therapy Med. Phys. 40 031708

Bertholet J et al. 2019 Real-time intrafraction motion monitoring in external beam radiotherapy Phys. Med. Biol. 64 15TR01

Boda-Heggemann J et al. 2016 Deep inspiration breath hold-based radiation therapy: a clinical review Int. J. Radiat. Oncol. Biol. Phys. 94 478–92 [PubMed: 26867877]

Cho B, Poulsen PR, Sawant A, Ruan D and Keall J 2011 Real-time target position estimation using stereoscopic kilovoltage/megavoltage imaging and external respiratory monitoring for dynamic multileaf collimator tracking Int. J. Radiat. Oncol. Biol. Phys. 79 269–78 [PubMed: 20615623]

Fayad H, Pan T, Clement JF and Visvikis D 2011 Technical note: correlation of respiratory motion between external patient surface and internal anatomical landmarks Med. Phys. 38 3157–64 [PubMed: 21815390]

Ferguson D et al. 2020 Markerless tumor tracking for VMAT Phys. Med. Biol. 65 125011

Gierga DP, Brewer J, Sharp GC, Betke M, Willett CG and Chen GTY 2005 The correlation between internal and external markers for abdominal tumors: implications for respiratory gating Int. J. Radiat. Oncol. Biol. Phys. 61 1551–8 [PubMed: 15817361]

Happersett L, Wang P, Zhang P, Mechalakos J, Li G, Eley E, Zelefsky M, Mageras G, Damato AL and Hunt M 2019 Developing a MLC modifier program to improve fiducial detection for MV/kV imaging during hypofractionated prostate volumetric modulated arc therapy J. Appl. Clin. Med. Phys. 20 120–4

Harris TC et al. 2020 Clinical translation of a new flat-panel detector for beam's-eye-view imaging Phys. Med. Biol. 65 225004 [PubMed: 33284786]

Heinzerling JH, Anderson JF, Papiez L, Boike T, Chien S, Geoffrey Z, Abdulrahman R and Timmerman R 2008 Four-dimensional computed tomography scan analysis of tumor and organ motion at varying levels of abdominal compression during stereotactic treatment of lung and liver Int. J. Radiat. Oncol. Biol. Phys. 70 1571–8 [PubMed: 18374231]

Herman MG, Balter JM, Jaffray DA, McGee KP, Munro P, Shalev S, Van Herk M and Wong JW 2001 Clinical use of electronic portal imaging: report of AAPM radiation therapy committee task group 58 Med. Phys. 28 712–37 [PubMed: 11393467]

Hu YH et al. 2018 Feasibility of closed-MLC tracking using high sensitivity and multi-layer electronic portal imagers Phys. Med. Biol. 63 235030

Hu YH, Myronakis M, Rottmann J, Wang A, Morf D, Shedlock D, Baturin P, Star-Lack J and Berbeco R 2017 A novel method for quantification of beam's-eye-view tumor tracking performance Med. Phys. 44 5650–9 [PubMed: 28887836]

Hu YH et al. 2019 Characterizing a novel scintillating glass for application to megavoltage cone-beam computed tomography Med. Phys. 46 1323–30 [PubMed: 30586163]

Ionascu D, Jiang SB, Nishioka S, Shirato H and Berbeco RI 2007 Internal-external correlation investigations of respiratory induced motion of lung tumors Med. Phys. 34 3893–903 [PubMed: 17985635]

Keall P, Todor AD, Vedam SS, Bartee CL, Siebers JV, Kini VR and Mohan R 2004 On the use of EPID-based implanted marker tracking for 4D radiotherapy Med. Phys. 31 3492–9 [PubMed: 15651632]

Keall PJ et al. 2006 The management of respiratory motion in radiation oncology report of AAPM task group 76 Med. Phys. 33 3874–900 [PubMed: 17089851]

Lu B, Chen Y, Park JC, Fan Q, Kahler D and Liu C 2015 A method of surface marker location optimization for tumor motion estimation in lung stereotactic body radiation therapy Med. Phys. 42 244–53 [PubMed: 25563264]

Ma T, Kilian-Meneghin J and Kumaraswamy L 2018 Recommendation of fiducial marker implantation for better target tracking using MV imager in prostate radiotherapy J. Appl. Clin. Med. Phys. 19 389–97 [PubMed: 29947073]

Mageras GS et al. 2004 Measurement of lung tumor motion using respiration-correlated CT Int. J. Radiat. Oncol. Biol. Phys. 60 933–41 [PubMed: 15465212]

Murphy MJ et al. 2007 The management of imaging dose during image-guided radiotherapy: report of the AAPM Task Group 75 Med. Phys. 34 4041–63 [PubMed: 17985650]

Park S-J, Ionascu D, Hacker F, Mamon H and Berbeco R 2009 Automatic marker detection and 3D position reconstruction using cine EPID images for SBRT verification Med. Phys. 36 4536–46 [PubMed: 19928085]

Star-Lack J et al. 2015 A piecewise-focused high DQE detector for MV imaging Med. Phys. 42 5084–99 [PubMed: 26328960]

Swank RK 1973 Absorption and noise in x-ray phosphors J. Appl. Phys. 44 4199–203

Wiersma RD, Mao W and Xing L 2008 Combined kV and MV imaging for real-time tracking of implanted fiducial markers Med. Phys. 35 1191–8 [PubMed: 18491510]

Wong JW, Sharpe MB, Jaffray DA, Kini VR, Robertson JM, Stromberg JS and Martinez AA 1999 The use of active breathing control (ABC) to reduce margin for breathing motion Int. J. Radiat. Oncol. Biol. Phys. 44 911–9 [PubMed: 10386650]

Yue Y, Aristophanous M, Rottmann J and Berbeco RI 2011 3-D fiducial motion tracking using limited MV projections in arc therapy Med. Phys. 38 3222–31 [PubMed: 21815397]

Zhao W, Ristic G and Rowlands JA 2004 X-ray imaging performance of structured cesium iodide scintillators Med. Phys. 31 2594–605 [PubMed: 15487742]

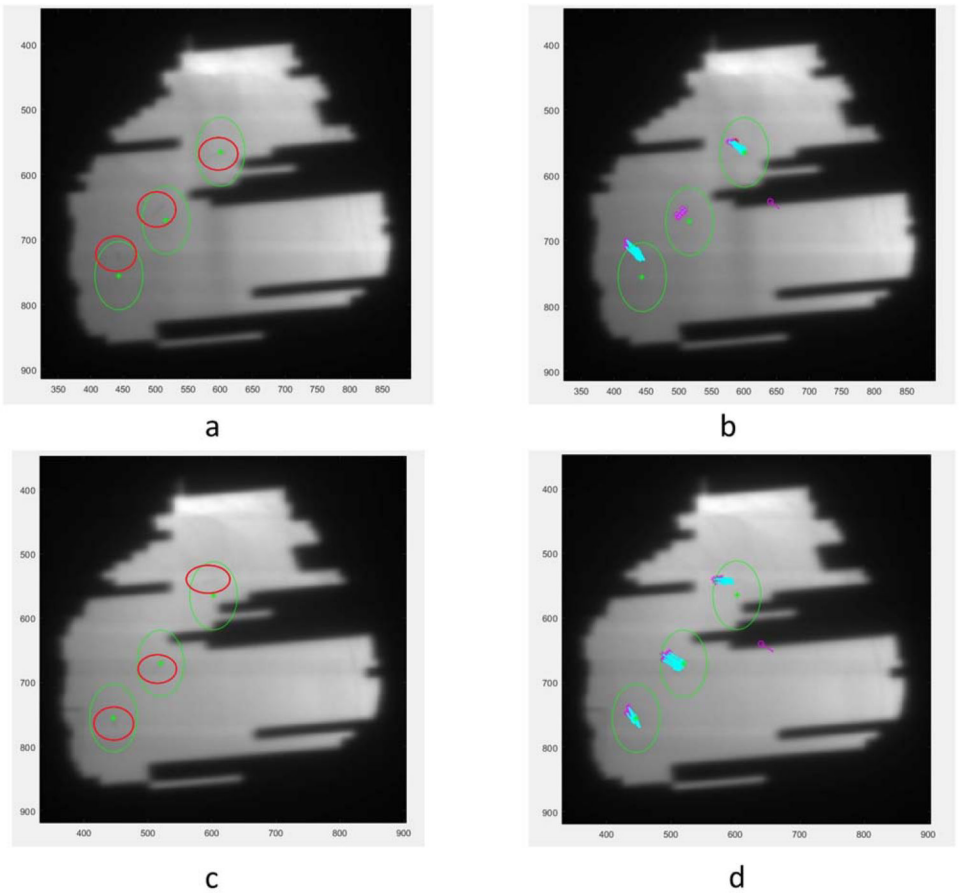

Figure 1.

(a). A sample 4-layer image. Green circles are fiducial search areas, red circles were drawn on to mark more clearly the actual fiducial locations. Numbers on the *x*- and *y*-axes are pixel positions on the EPID. (b). The same 4-layer image with tracking information. Purple asterisks show the most recent new generation of templates around a fiducial after a frame without tracking and the blue arrows point to the current templates' locations. (c). Corresponding 1-layer image without tracking information. (d). Corresponding 1-layer image with tracking information.

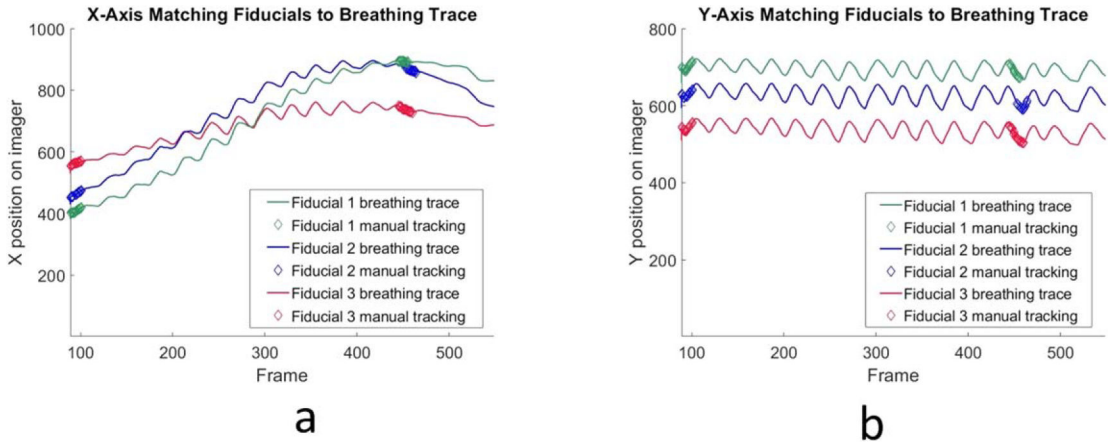

Figure 2.

(a). Manually matched fiducials' *X* coordinate on MLI images shown as thicker overlapping diamond points near the beginning of data acquisition and near the end are overlaid with the full breathing trace displayed as a continuous line. Acquisition was manually triggered and the initial empty frames omitted, thus the first frame is not '1'. (b). Manually matched fiducials' *Y* coordinate.

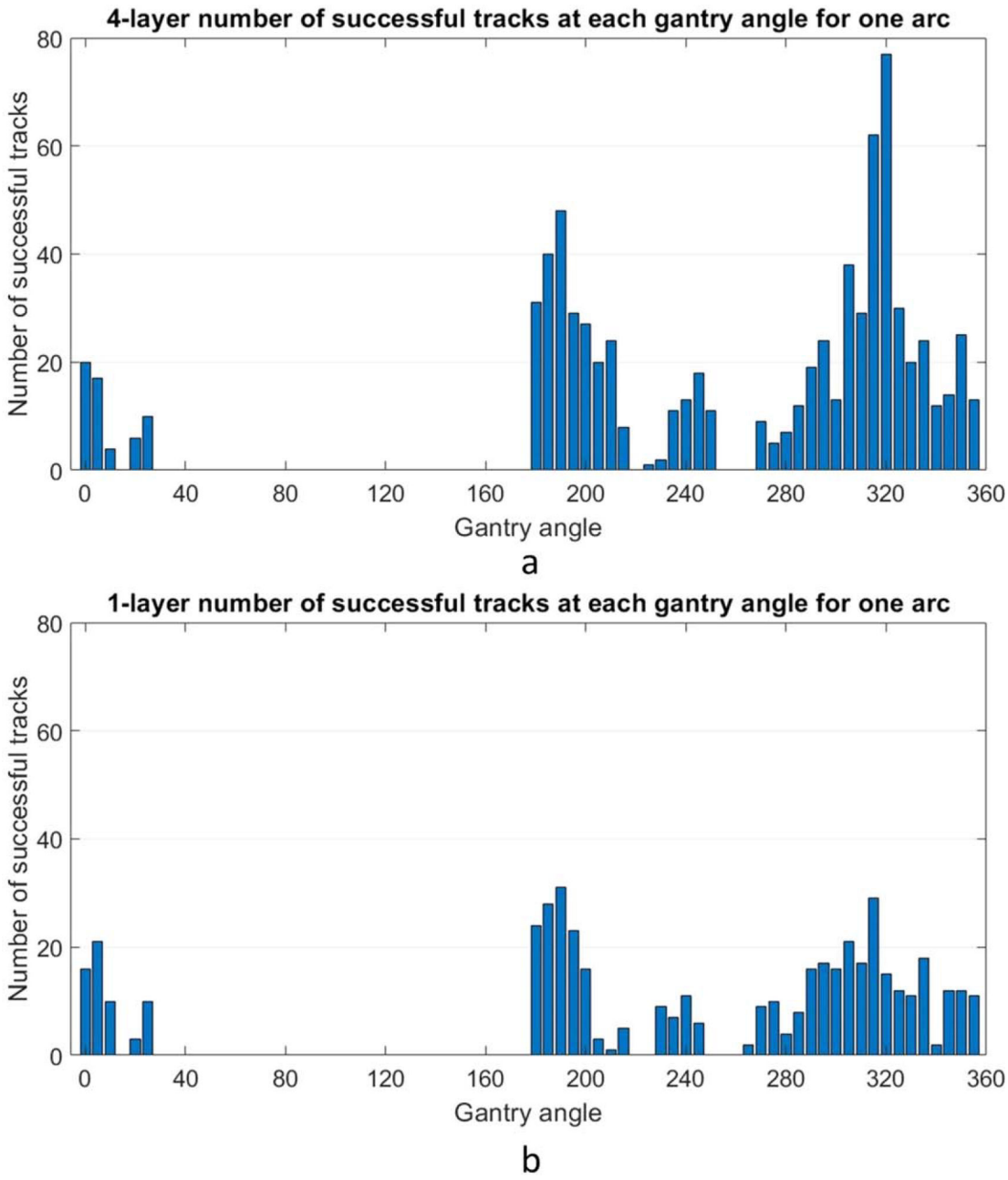

Figure 3.

(a). Example gantry angle locations of successfully tracked frames for one patient's arc in 5 degree bins, with the MLI in 4-layer mode. Note that for this patient no arcs covered the range from 30 to 180. (b). The same analysis is shown for the same patient/arc in 1-layer mode.

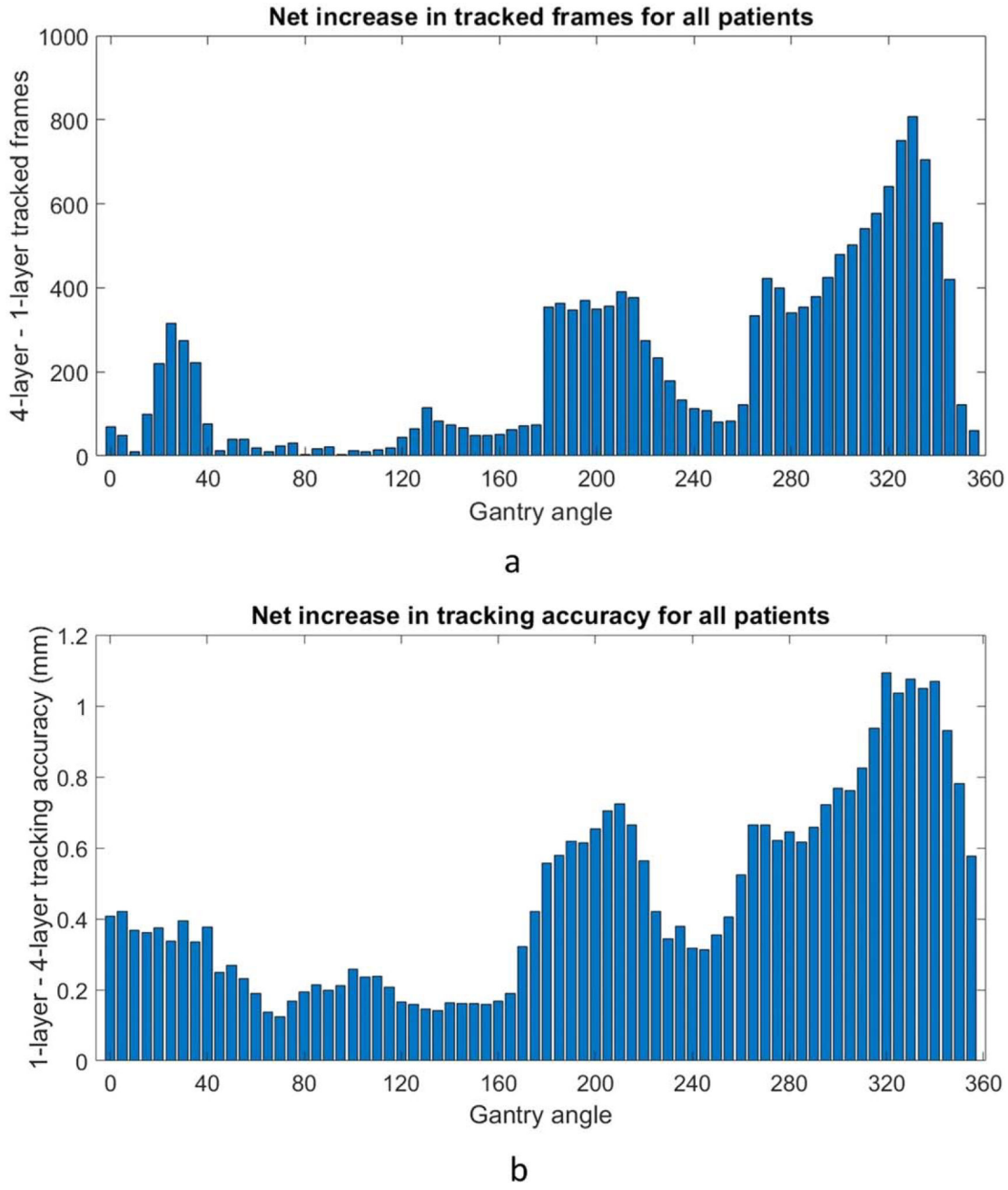

Figure 4.

(a). The net increase of tracked frames over all the data utilizing the 4-layer mode at different gantry angles, using 5 degree bins. Most patients did not have arcs between 30 and 180 degrees, explaining the lack of data in that range. (b). The net increase in tracking accuracy RMSE at different gantry angles.

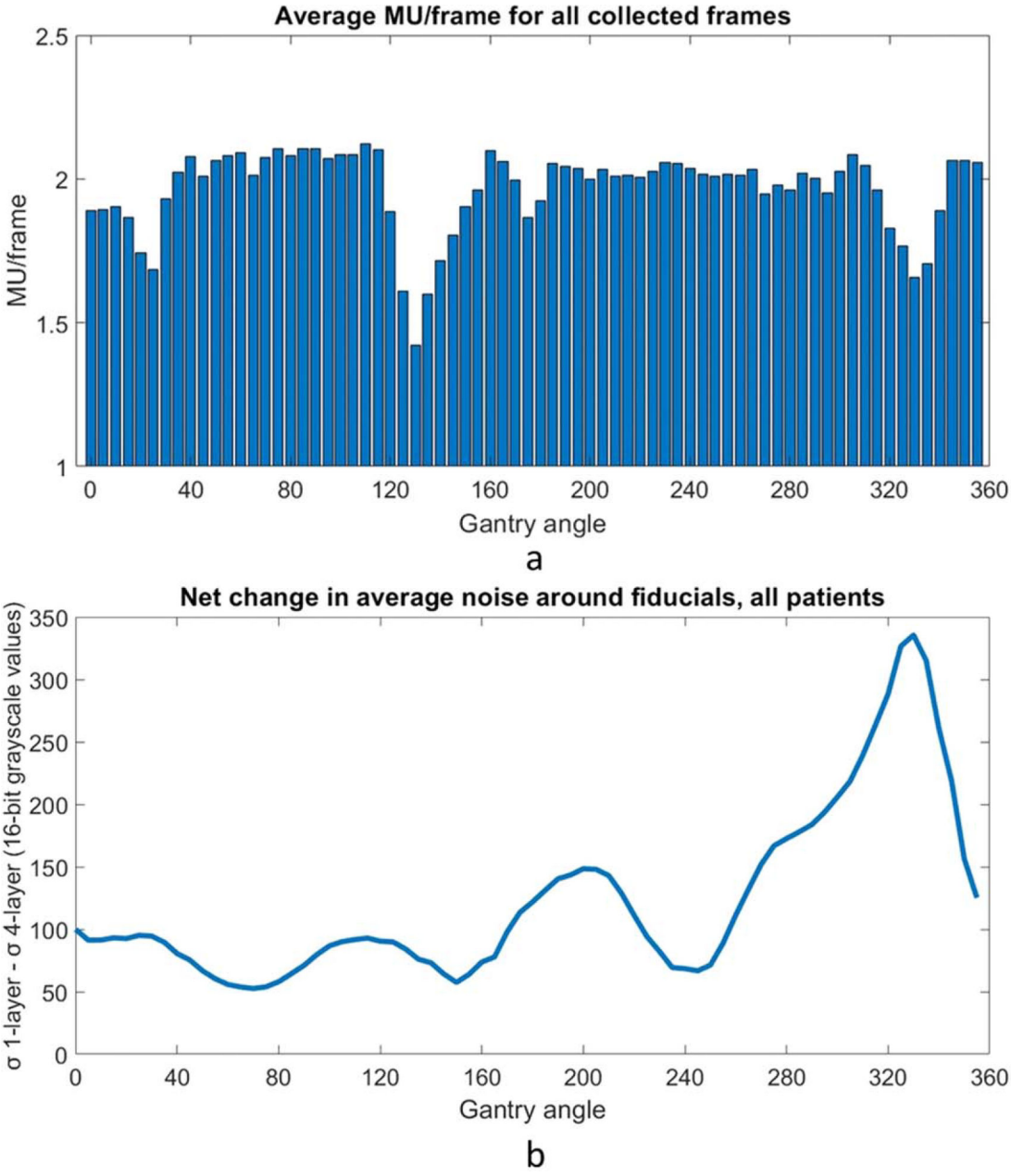

Figure 5.

(a). MU/frame as a function of gantry angle in 5 degree bins across all data. Data was acquired at around 10.1 frames per second, so the max value corresponding to the nominal maximum dose rate for a 6FFF beam of 1400 MU min^{-1} is 2.3 MU/frame. Consistent dips in dose rate are observed at around gantry 130 and gantry 330. (b). Decrease in noise around the expected fiducial location when using the MLI in 4-layer mode as a function of gantry angle. There is a peak centered around a gantry angle of 330 degrees.

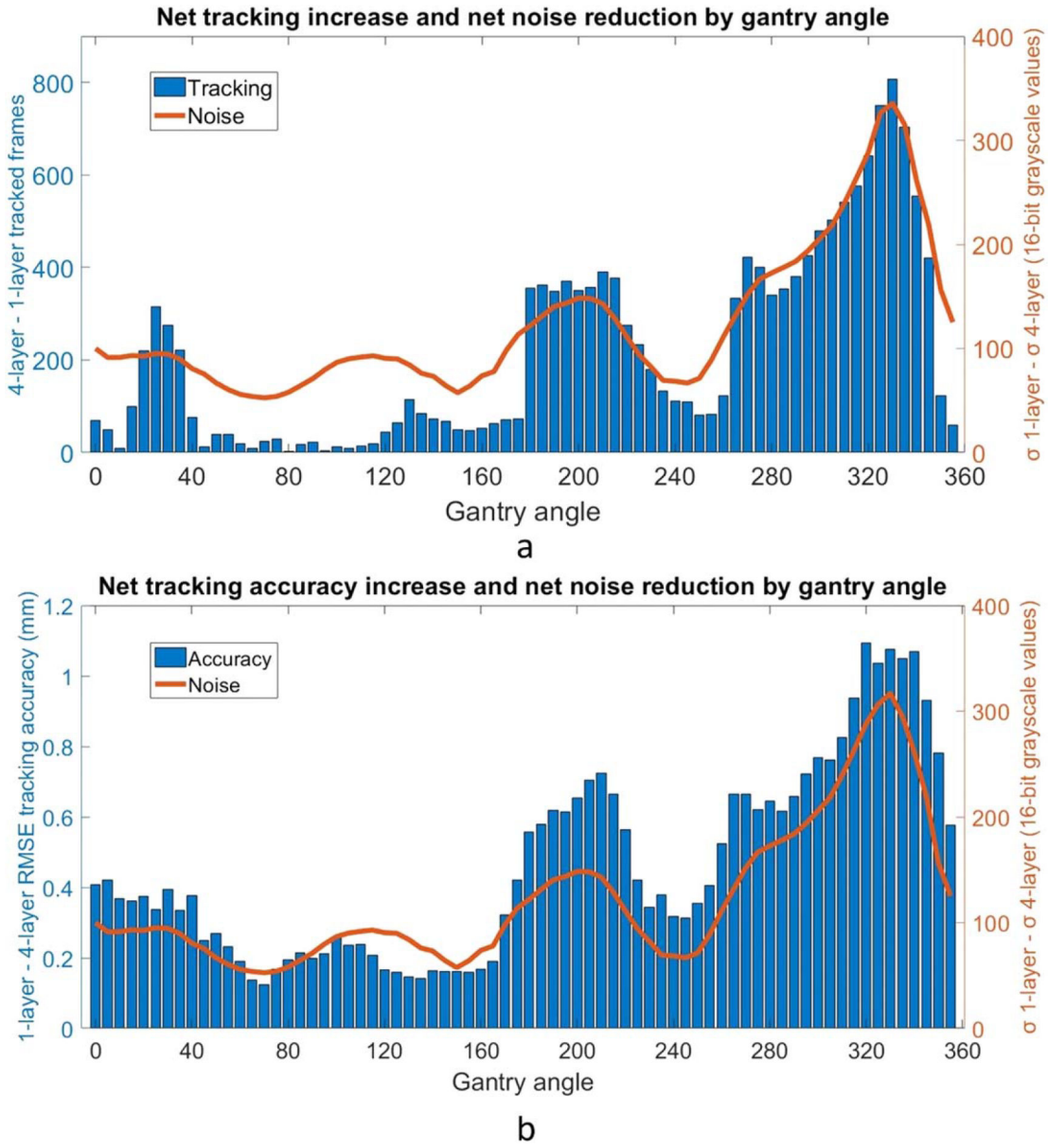

Figure 6.

(a). Combined plot showing increased tracking efficiency using 4 layers in blue overlaid with the image noise reduction using 4 layers in orange. Minimal data in the gantry angle range of 30–180 degrees suppresses the net change in tracked frames. Overall, there is a correlation coefficient of $r = 0.913$, suggesting that the noise reduction of the 4-layer acquisition is correlated with improved tracking performance. (b). Combined plot showing increased tracking accuracy RMSE using 4 layers in blue overlaid with the image noise reduction using 4 layers in orange. There is a correlation coefficient of $r = 0.927$, suggesting an additional correlation between noise reduction and tracking accuracy improvement.

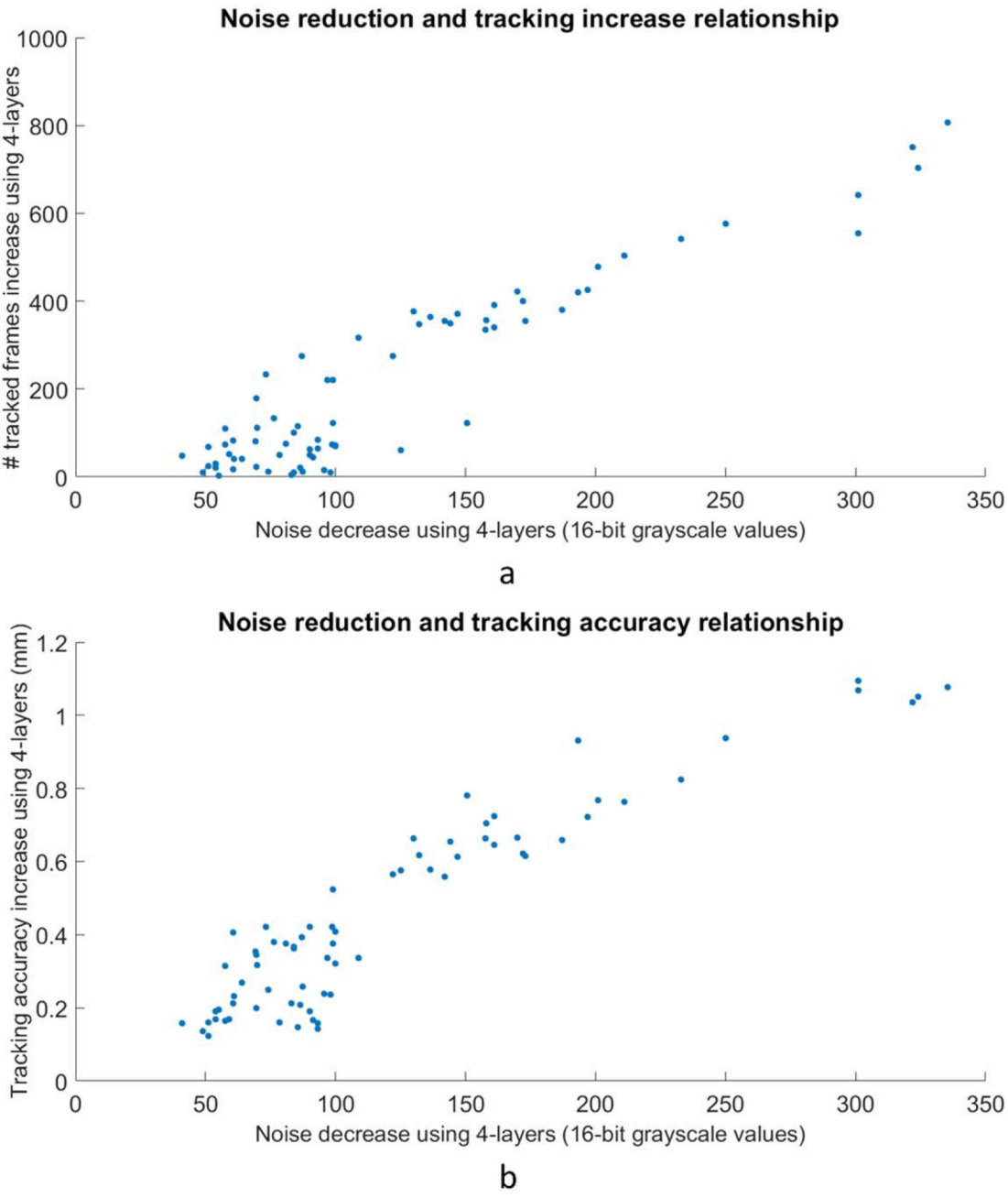

Figure 7.

(a). The data from figure 6(a) replotted as tracking increase as a function of noise decrease. A correlation between decreased noise and increased tracking can be observed. (b). Figure 6(b) data replotted with tracking accuracy increase as a function of noise decrease.

Table 1.

Tracking results for all of patients, each arc, are shown. 4-layer mode results in more accurate and more efficient tracking ($p < 0.001$).

		2D tracking error and tracking efficiency by patient arc							
		Patient 1	**Patient 2**	**Patient 3**	**Patient 4**	**Patient 5**	**Patient 6**	**Mean**	**Delta**
Tracking RMSE (mm)	4-layer	1.36	1.65	1.61	1.53	1.32	1.26	1.5	0.6 $p < 0.001$
	1-layer	2.11	2.28	2.52	2.03	1.80	1.76	2.1	
Tracking efficiency	4-layer	84.4%	88.7%	83.4%	79.7%	84.9%	75.2%	82.8%	41.7% $p < 0.001$
	1-layer	55.7%	64.4%	59.3%	58.3%	59.6%	55.5%	58.4%	